The Journal of Chemical Physics

RESEARCH ARTICLE | OCTOBER 12 2023

Predicting rate kernels via dynamic mode decomposition

Special Collection: 2023 JCP Emerging Investigators Special Collection

Wei Liu ; Zi-Hao Chen ; Yu Su ; Yao Wang ; Wenjie Dou

J. Chem. Phys. 159, 144110 (2023)
https://doi.org/10.1063/5.0170512

The Journal of Chemical Physics ARTICLE pubs.aip.org/aip/jcp

Predicting rate kernels via dynamic mode decomposition

Cite as: J. Chem. Phys. 159, 144110 (2023); doi: 10.1063/5.0170512
Submitted: 3 August 2023 • Accepted: 25 September 2023 •
Published Online: 12 October 2023

Wei Liu,[1,2] Zi-Hao Chen,[3] Yu Su,[3] Yao Wang,[3,a)] and Wenjie Dou[1,2,4,b)]

AFFILIATIONS

[1] Department of Chemistry, School of Science, Westlake University, Hangzhou 310024 Zhejiang, China
[2] Institute of Natural Sciences, Westlake Institute for Advanced Study, Hangzhou 310024 Zhejiang, China
[3] Department of Chemical Physics, University of Science and Technology of China, Hefei, Anhui 230026, China
[4] Department of Physics, School of Science, Westlake University, Hangzhou 310024, Zhejiang, China

Note: This paper is part of the 2023 JCP Emerging Investigators Special Collection.
[a)] **E-mail:** wy2010@ustc.edu.cn
[b)] **Author to whom correspondence should be addressed:** douwenjie@westlake.edu.cn

ABSTRACT

Simulating dynamics of open quantum systems is sometimes a significant challenge, despite the availability of various exact or approximate methods. Particularly when dealing with complex systems, the huge computational cost will largely limit the applicability of these methods. In this work, we investigate the usage of dynamic mode decomposition (DMD) to evaluate the rate kernels in quantum rate processes. DMD is a data-driven model reduction technique that characterizes the rate kernels using snapshots collected from a small time window, allowing us to predict the long-term behaviors with only a limited number of samples. Our investigations show that whether the external field is involved or not, the DMD can give accurate prediction of the result compared with the traditional propagations, and simultaneously reduce the required computational cost.

I. INTRODUCTION

Dynamic mode decomposition (DMD) was introduced by Schmid[1] in fluid dynamics to study spatio-temporal coherent structures from high-dimensional data. Built upon the proper orthogonal decomposition (POD) and the singular value decomposition (SVD), DMD method aims to efficiently reduce the dimensionality of complex systems. Different from the original POD or SVD which disregards the temporal information, DMD offers a modal decomposition method which not only achieves the dimensionality reduction but also produces the dynamical behaviors of these modes. Shortly after the initial development of the DMD algorithm,[1] Rowley, Mezic, and their collaborators established the connection between the DMD and the Koopman's theory.[2] Seeking to identify the most suitable temporal frequencies and spatial modes,[3] DMD essentially serves as an approximation to the Koopman's operator which governs the dynamics of a high-dimensional system. Using the linear DMD framework to study nonlinear dynamical systems has attracted a lot of research interest over the past years.[4] Recently, DMD has emerged as a versatile algorithm for the data-driven characterization of high-dimensional systems. This algorithm is applicable to both experimental and numerical data, and combines the advantageous features of the SVD for spatial dimensionality reduction and the Fast Fourier Transform (FFT) for identifying temporal frequencies.[4,5] Consequently, each DMD mode corresponds to a distinct eigenvalue $\lambda = a + ib$, wherein b denotes the oscillation frequency and a represents the rate of growth or decay.

It is a natural and attractive idea to use the DMD method for simulating dynamics of complex quantum systems, since DMD does provide real-time and real space information. Note that DMD has been used in real-time time-dependent density functional theory (TDDFT) calculations.[6] As known, simulating open quantum systems is a significant challenge, despite the availability various exact or approximate methods, such as the quantum jump operator method,[7] the quantum master equation,[8–15] the quantum random walk method,[16] the quantum Monte Carlo method,[17–19] the machine learning time-local generators,[20] and the dissipaton equation of motion (DEOM).[21–24] The DEOM serves as the benchmark method exploited in this work, which is the second quantization generalization of the well-known hierarchical equations of motion (HEOM).[10,25–36] Employing the linear space algebra, DEOM enables

the utilization of the Nakajima-Zwanzig projection operator technique. This technique allows for a focus on the dynamics of specific subspaces and the construction of non-Markovian rate kernels.[9,37,38] However, when dealing with complex systems, the huge computational cost will largely limit the applicability of these methods. For example, the computational bottleneck emerges when calculating the non-Markovian rate kernels in DEOM simulations, especially for large systems at low temperatures. To overcome this shortcoming, we use the DMD algorithm to compute snapshots of non-Markovian rate kernels within short span of time and subsequently predict the rate kernel information for the entire time window. This approach significantly reduces the computational resource required for simulating the quantum rate processes.

The remainder of this paper is organized as follows. Section II provides an overview of the theoretical framework of the DMD method, followed by the introduction of the Hamiltonian for the electron transfer system, as well as the rate kernels. In Sec. III, we present the numerical results for the rate kernels, population or coherence dynamics, exemplified with the non-Markovian processes in both the time-independent and the Floquet scenarios. Finally, we summarize our paper in Sec. IV.

II. THEORY

A. Dynamic mode decomposition

In this section, we provide a concise overview of the fundamental principles underlying the DMD technique, as well as the numerical procedures for implementing this method.

DMD is a data-driven technique to extract significant spatial modes and temporal frequencies from a nonlinear dynamical system to reduce the large number of degrees of freedom.[1,4,39,40] The extracted modes and frequencies are then used to predict the future states of the nonlinear system. To be more explicit, let us consider a dynamical system governed by the following nonlinear ordinary differential equation:

$$\frac{d\mathbf{x}(t)}{dt} = \mathbf{f}(\mathbf{x}(t), t), \quad t \geq 0. \tag{1}$$

Here, $\mathbf{x}(t) := [x_1(t), x_2(t), \ldots, x_n(t)]^T \in \mathbb{C}^n$ is the time-dependent state variable, and $\mathbf{f} : \mathbb{C}^n \otimes \mathbb{R}^+ \to \mathbb{C}^n$ is a nonlinear function of $\mathbf{x}$ and time t. Here, $\mathbf{x}(t)$ is the observable of interest, which can be our rate kernels as shown below. The overall goal of DMD is to identify a collection of time-independent spatial modes $\phi_1, \phi_2, \ldots, \phi_k$ alongside a set of temporal frequencies $\omega_1, \omega_2, \ldots, \omega_k$ to approximate $\mathbf{x}(t)$:

$$\mathbf{x}(t) \approx \sum_{\ell=1}^{r} \beta_\ell \phi_\ell e^{i\omega_\ell t}, \tag{2}$$

where β_ℓ is a set of coefficients and r is the rank (which is relatively small). In practice, the trajectory $\mathbf{x}(t)$ is not known before solving Eq. (1). We now explain how to obtain the most significant values of ϕ_i and ω_i from a limited number of snapshots (or samples) of $\mathbf{x}(t)$ that we can solve.

To obtain the dynamic modes ϕ_ℓ and their corresponding frequencies ω_ℓ, we first map the trajectories of the nonlinear dynamics to a linear system, which can be characterized easily through a spectral decomposition of the linear operator. This strategy is referred to as Koopman theory.[2,41–46] To be more explicit, a scalar observable $g(\mathbf{x}(t))$ within a small time interval ($\Delta t > 0$) for a dynamical system described by Eq. (1) can be characterized as

$$g(\mathbf{x}(t + \Delta t)) = \mathcal{K}_{\Delta t} g(\mathbf{x}(t)). \tag{3}$$

Here, $\mathcal{K}_{\Delta t}$ is a linear operator that is independent of both the time parameter and the choice of the observable function g. In general, $\mathcal{K}_{\Delta t}$ is an infinite-dimensional linear operator that has an infinite number of eigenvalues $\{\lambda_i\}$ and eigenfunctions $\{\varphi_i(\mathbf{x})\}$ satisfy $\varphi_i(\mathbf{x}(t + \Delta t)) = \mathcal{K}_{\Delta t}\varphi_i(\mathbf{x}(t)) = \lambda_i \varphi_i(\mathbf{x}(t))$. If a set of n observable functions $g_j(\mathbf{x}(t))$, $j = 1, 2, \ldots, n$ is contained in such an invariant subspace of $\mathcal{K}_{\Delta t}$, then there are vectors $v_1, v_2, \ldots, v_n \in \mathbb{C}^n$, such that

$$\begin{bmatrix} g_1(\mathbf{x}(t)) \\ g_2(\mathbf{x}(t)) \\ \cdot \\ \cdot \\ \cdot \\ g_n(\mathbf{x}(t)) \end{bmatrix} = \begin{bmatrix} v_1 & v_2 \cdots v_n \end{bmatrix} \begin{bmatrix} \varphi_1(\mathbf{x}(t)) \\ \varphi_2(\mathbf{x}(t)) \\ \cdot \\ \cdot \\ \cdot \\ \varphi_n(\mathbf{x}(t)) \end{bmatrix}. \tag{4}$$

Here $\varphi_1(\mathbf{x}), \ldots, \varphi_n(\mathbf{x})$ and $\lambda_1, \ldots, \lambda_n$ are the eigenfunctions and eigenvalues of $\mathcal{K}_{\Delta t}$ that span a subspace with $n \in \mathbb{N}^+$ the dimension. Thus, the expansion of the observable function in Eq. (4) can be thought of as a change of basis into eigenfunction coordinates.

In particular, if $g_j(\mathbf{x}(t))$ is the jth component of $\mathbf{x}(t)$, i.e., $g_j(\mathbf{x}(t)) = x_j(t)$, we have

$$\mathbf{x}(t + \Delta t) = \begin{bmatrix} \mathcal{K}_{\Delta t} x_1(t) \\ \mathcal{K}_{\Delta t} x_2(t) \\ \cdot \\ \cdot \\ \cdot \\ \mathcal{K}_{\Delta t} x_n(t) \end{bmatrix} = \begin{bmatrix} \lambda_1 v_1 & \lambda_2 v_2 \cdots \lambda_n v_n \end{bmatrix} \begin{bmatrix} \varphi_1(\mathbf{x}(t)) \\ \varphi_2(\mathbf{x}(t)) \\ \cdot \\ \cdot \\ \cdot \\ \varphi_n(\mathbf{x}(t)) \end{bmatrix} = \mathbf{A}\mathbf{x}(t), \tag{5}$$

Here, we have defined

$$\mathbf{A} = \begin{bmatrix} \lambda_1 v_1 & \lambda_2 v_2 \cdots \lambda_n v_n \end{bmatrix} \begin{bmatrix} v_1 & v_2 \cdots v_n \end{bmatrix}^\dagger \in \mathbb{C}^{n \times n}, \tag{6}$$

where $(\cdot)^\dagger$ denotes the Moore-Penrose pseudoinverse. As a result, the dynamical system of $\mathbf{x}(t)$ is completely governed by $\mathbf{A}$, which is the main object of interest. Notice that the Koopman operator $\mathcal{K}_{\Delta t}$ is not known in advance. Below, we offer the procedures to approximate $\mathbf{A}$.

Suppose we have a sample of predetermined snapshots of $\mathbf{x}(t)$, we can approximate $\mathbf{A}$ using these snapshots. We take the uniformly distributed samples at $t_i = t_1 + (i - 1)\Delta t$ (where $i = 1, \ldots, m$), such that the snapshots are represented as $\mathbf{x}_i = \mathbf{x}(t_i)$. We then determine $\mathbf{A}$ by minimizing the Frobenius norm of $\mathbf{R}(\mathbf{A})$, which is defined as

$$\mathbf{R}(\mathbf{A}) = \mathbf{A}\mathbf{X}_1 - \mathbf{X}_2. \tag{7}$$

Here, $\mathbf{X}_1 = (\mathbf{x}_1\mathbf{x}_2 \ldots \mathbf{x}_{m-1})$ and $\mathbf{X}_2 = (\mathbf{x}_2\mathbf{x}_3 \ldots \mathbf{x}_m)$. The least squares solution to $\min_A \|\mathbf{R}(\mathbf{A})\|_F$ (where $\|\cdot\|_F$ denotes the Frobenius norm) is

$$\mathbf{A} = \mathbf{X}_2\mathbf{X}_1^{\dagger}. \tag{8}$$

The pseudoinverse $\mathbf{X}_1^{\dagger}$ can be obtained from the singular value decomposition (SVD)[47] of $\mathbf{X}_1$, *i.e.*

$$\mathbf{X}_1 = \mathbf{U}\Sigma\mathbf{V}^*, \tag{9}$$

with $\mathbf{U} \in \mathbb{C}^{n\times n}$, $\Sigma \in \mathbb{C}^{n\times m}$, $\mathbf{V} \in \mathbb{C}^{m\times m}$ and $(\cdot)^*$ denotes the conjugate transpose. Here we have $\mathbf{U}^*\mathbf{U} = \mathbf{I}$ and $\mathbf{V}^*\mathbf{V} = \mathbf{I}$.

In many cases, singular values on the diagonal of $\mathbf{\Sigma}$ decay rapidly, such that the rank of $\mathbf{\Sigma}$ is small compared to the dimension of the $\mathbf{X}_1$, i.e. $r \ll \min\{n, m\}$. We can then define the projection matrices:

$$\tilde{\mathbf{U}} = \mathbf{U}(:, 1:r), \tilde{\Sigma} = \Sigma(1:r, 1:r), \tilde{\mathbf{V}} = \mathbf{V}(:, 1:r). \tag{10}$$

Using the projection matrices, we can map original $\mathbf{A}$ matrix into a r-rank matrix $\tilde{\mathbf{A}}$:

$$\tilde{\mathbf{A}} = \tilde{\mathbf{U}}^*\mathbf{A}\tilde{\mathbf{U}} \approx \tilde{\mathbf{U}}^*\mathbf{X}_2\tilde{\mathbf{V}}\tilde{\Sigma}^{-1}\tilde{\mathbf{U}}^*\tilde{\mathbf{U}} = \tilde{\mathbf{U}}^*\mathbf{X}_2\tilde{\mathbf{V}}\tilde{\Sigma}^{-1}. \tag{11}$$

We have used the low-rank approximation in the above equation, i.e. $\mathbf{X}_1 \approx \tilde{\mathbf{U}}\tilde{\Sigma}\tilde{\mathbf{V}}^*$.

To proceed, we solve the eigenvalue problem of the reduced matrix:

$$\tilde{\mathbf{A}}\mathbf{W} = \mathbf{W}\Lambda, \tag{12}$$

where Λ is the eigenvalue matrix,

$$\Lambda = \begin{bmatrix} \lambda_1 & & \\ & \ddots & \\ & & \lambda_r \end{bmatrix} \tag{13}$$

and matrix $\mathbf{W}$ is the corresponding eigenvectors. To further represent the dynamical system in the form of Eq. (2), we can redefine the eigenvalue matrix:

$$\mathbf{\Omega} = \frac{\ln \Lambda}{\Delta t} = \begin{bmatrix} \mathrm{i}\omega_1^{\mathrm{DMD}} & & \\ & \ddots & \\ & & \mathrm{i}\omega_r^{\mathrm{DMD}} \end{bmatrix}, \tag{14}$$

where $\omega_l^{\mathrm{DMD}} = -\mathrm{i}\frac{\ln \lambda_\ell}{\Delta t}$, for $\ell = 1, \ldots, r$. In addition, to obtain spectral modes in the original state space of $\mathbb{C}^n$, we perform the following transformation:

$$\Phi = \mathbf{X}_2\tilde{\mathbf{V}}\tilde{\Sigma}^{-1}\mathbf{W}. \tag{15}$$

where the columns of Φ are referred to as the DMD modes. Such that the dynamical system $\mathbf{x}$ can be approximated by:

$$\mathbf{x}(t) \approx \Phi \exp(\mathbf{\Omega}t)\mathbf{b} = \sum_{\ell=1}^{r} \phi_\ell \exp\left(\mathrm{i}\omega_\ell^{\mathrm{DMD}} t\right) b_\ell. \tag{16}$$

The amplitude vector $\mathbf{b}$ in the above equation is left to be determined. There are two approaches to calculate $\mathbf{b}$. The first approach determines $\mathbf{b}$ directly by taking the projection of the initial value $\mathbf{x}_1$ onto the DMD modes using the matrix $\Phi^{\dagger}$:

$$\mathbf{b} = \Phi^{\dagger}\mathbf{x}_1, \tag{17}$$

Alternatively, $\mathbf{b}$ can be computed as the least squares fit of the approximated DMD modes on the sampled trajectories. To be more explicit, we minimize the difference between the expression $\Phi \exp(\Omega t_j)\mathbf{b}$ and the observed data $\mathbf{x}_j$ over a set of m sampled time points.

$$\mathbf{b} = \arg\min_{\tilde{\mathbf{b}}\in\mathbb{C}^n} \sum_{i=1}^{m} \|\Phi \exp(\mathbf{\Omega}t_i)\tilde{\mathbf{b}} - \mathbf{x}_i\|_{l^2}^2, \tag{18}$$

where $\|\cdot\|_{l^2}$ denotes the standard Euclidean norm of a vector.

The description of the DMD procedure indicates that the primary computational expense arises from the SVD calculation described in Eq. (9), with a complexity of $O(\min(m^2n, nm^2))$. Note that DMD does not require knowledge of the underlying dynamics given by the function $\mathbf{f}(\mathbf{x}(t), t)$ in Eq. (1). Instead, DMD utilizes data from the initial time steps and predicts the future states of the system. Additionally, DMD reduces the computational cost by projecting the n-dimensional space into r-dimensional subspace. Thus, this method is useful for analyzing nonlinear or high-dimensional dynamical systems.

B. Model Hamiltonian

In this subsection, we introduce the electron transfer system that will be used in the following sections. Let us consider a donor-bridge-acceptor system for electron transfer, whose Hamiltonian reads,[48]

$$\begin{aligned} H_{\mathrm{T}} = {} & h_{\mathrm{D}}|\mathrm{D}\rangle\langle\mathrm{D}| + (E^{\circ} + h_{\mathrm{A}})|\mathrm{A}\rangle\langle\mathrm{A}| + H_{\mathrm{B}} \\ & + V(\{\tilde{q}_k\})(|\mathrm{D}\rangle\langle\mathrm{A}| + |\mathrm{A}\rangle\langle\mathrm{D}|). \end{aligned} \tag{19}$$

Here, E° represents the standard reaction Gibbs energy for the electron transfer process from the donor state ($|\mathrm{D}\rangle$) to the acceptor state ($|\mathrm{A}\rangle$). The donor state and the acceptor state are each influenced by their respective solvent environments, h_{D} and h_{A}. Specifically, h_{D} can be described as $h_{\mathrm{D}} = \sum_j \frac{\omega_j}{2}(p_j^2 + x_j^2)$, while h_{A} is given by $h_{\mathrm{A}} = \sum_j \frac{\omega_j}{2}[p_j^2 + (x_j - d_j)^2]$. In Eq. (19), $V(\{\tilde{q}_k\})$ depends on the coordinates of the bridge, and the Hamiltonian for the fluctuating bridges can be expressed as $H_{\mathrm{B}} = \sum_k \frac{\tilde{\omega}_k}{2}(\tilde{p}_k^2 + \tilde{q}_k^2)$. Initially, the total density operator can be represented as $\rho_{\mathrm{T}}(t_0) = |\mathrm{D}\rangle\langle\mathrm{D}| \otimes (e^{-\beta h_{\mathrm{D}}}/\mathrm{tr}e^{-\beta h_{\mathrm{D}}}) \otimes (e^{-\beta H_{\mathrm{B}}}/\mathrm{tr}e^{-\beta H_{\mathrm{B}}})$, which denotes the thermal equilibrium in the donor state, with $\beta = 1/(k_B T)$ being the inverse temperature.

We also consider the presence of external periodic driving, which is referred to as the Floquet scenario. In this case,

$$E^{\circ} \to E(t) = E^{\circ} + \varepsilon \cos \Omega t, \tag{20}$$

with ε being the driving amplitude and Ω the driving frequency.

The Hamiltonian in Eq. (19) can be decomposed into the system and the environment as follows:[48]

$$H_{\mathrm{T}} = H_{\mathrm{S}} + h_{\mathrm{E}} - |\mathrm{A}\rangle\langle\mathrm{A}|\delta\hat{U} - \hat{Q}\delta\hat{V} \tag{21}$$

Here $h_E = h_D + H_B$ is the Hamiltonian for the environment, $\hat{Q}$ is defined as $\hat{Q} = |D\rangle\langle A| + |A\rangle\langle D|$, and the system Hamiltonian is given by

$$H_S = (E^\circ + \varepsilon \cos\Omega t + \lambda)|A\rangle\langle A| + \langle V\rangle_B(|D\rangle\langle A| + |A\rangle\langle D|). \quad (22)$$

In Eqs. (21) and (22), $\delta\hat{U} \equiv \hat{U} - \langle\hat{U}\rangle_D$ with $\hat{U} \equiv h_A - h_D$ and $\langle\hat{U}\rangle_D \equiv \mathrm{tr}_D(\hat{U}e^{-\beta h_D})/\mathrm{tr}_D(e^{-\beta h_D})$, whereas $\delta\hat{V} \equiv \langle V\rangle_B - V(\{\tilde{q}_k\}) = \sum_k \tilde{c}_k \tilde{q}_k$ with $\langle V\rangle_B \equiv \mathrm{tr}_B(Ve^{-\beta H_B})/\mathrm{tr}_B(e^{-\beta H_B})$.

In the simulations, we incorporate the spectral densities, $J_D(\omega) \equiv (1/2)\int_{-\infty}^{\infty} dt e^{i\omega t}\langle[\delta\hat{U}(t), \delta\hat{U}(0)]\rangle_D$ and $J_B(\omega) \equiv (1/2)\int_{-\infty}^{\infty} dt e^{i\omega t}\langle[\delta\hat{V}(t), \delta\hat{V}(0)]\rangle_B$, as[49–51]

$$J_D(\omega) = \frac{2\lambda\gamma\omega}{\omega^2 + \gamma^2} \quad (23)$$

and

$$J_B(\omega) = \frac{2\lambda'\omega_0^2\zeta\omega}{(\omega^2 - \omega_0^2)^2 + \omega^2\zeta^2}, \quad (24)$$

respectively.

C. Rate kernel calculation

In this subsection, we present the DEOM of the rate kernels. From a theoretical perspective, it is possible to precisely construct the generalized rate equation as

$$\dot{P}_D(t) = -\int_0^t d\tau k(t-\tau;t)P_D(\tau) + \int_0^t d\tau k'(t-\tau;t)P_A(\tau). \quad (25)$$

Here, $P_D(t)$ and $P_A(t)$ denote the populations of the donor and acceptor, respectively. Here, we employ the forward and backward rate memory kernels, $k(\tau;\ t)$ and $k'(\tau;\ t)$, in the rate equation. τ is the memory time scale, capturing the non-Markovian nature of the system. Note that t in $k(\tau;\ t)$ and $k'(\tau;\ t)$ represents the time dependence of the rate kernels due to the presence of an external field. These rate kernels are regularly calculated and examined to investigate the memory effect in rate processes.[38,52–55]

The rate kernels are constructed using the generalized master equation.[38] Based on the composite Hamiltonian in Eq. (19), the DEOM can be expressed as

$$\dot{\boldsymbol{\rho}}(t) = -i\boldsymbol{\mathcal{L}}(t)\boldsymbol{\rho}(t). \quad (26)$$

This equation is similar to the time evolution equation for the total system, $\dot{\rho}_T = -i\mathcal{L}_T(t)\rho_T$, despite that the total Liouvillian $\mathcal{L}_T(t)$ is mapped to the DEOM-space dynamics generator $\boldsymbol{\mathcal{L}}(t)$, and the total density matrix $\rho_T(t)$ is mapped to the DEOM density matrix $\boldsymbol{\rho}(t) = \{\rho_{\mathbf{n}}^{(n)}(t); n = 0, 1, 2, \ldots\}$. Here, $\mathcal{L}_T(t) \equiv [H_T(t), \cdot]$. To proceed, we define the projection operators in DEOM space, $\boldsymbol{\mathcal{P}}$ and $\boldsymbol{\mathcal{Q}} = \boldsymbol{\mathcal{I}} - \boldsymbol{\mathcal{P}}$, to separate $\boldsymbol{\rho}$ into its population and coherence components:[38]

$$\begin{aligned}\boldsymbol{\mathcal{P}}\boldsymbol{\rho}(t) &= \left\{\sum_a \rho_{aa}^{(0)}(t)|a\rangle\langle a|;\ 0,\ 0,\ \cdots\right\} \equiv \boldsymbol{p}(t)\\ \boldsymbol{\mathcal{Q}}\boldsymbol{\rho}(t) &= \left\{\sum_{a\neq b} \rho_{ab}^{(0)}(t)|a\rangle\langle b|; \rho_{\mathbf{n}}^{(n>0)}(t)\right\} \equiv \boldsymbol{\sigma}(t).\end{aligned} \quad (27)$$

We can now express the DEOM in Eq. (26) in a different form by using the following matrix representation:

$$\begin{bmatrix}\dot{\boldsymbol{p}}(t)\\ \dot{\boldsymbol{\sigma}}(t)\end{bmatrix} = -i\begin{bmatrix}\boldsymbol{\mathcal{P}}\boldsymbol{\mathcal{L}}(t)\boldsymbol{\mathcal{P}} & \boldsymbol{\mathcal{P}}\boldsymbol{\mathcal{L}}(t)\boldsymbol{\mathcal{Q}}\\ \boldsymbol{\mathcal{Q}}\boldsymbol{\mathcal{L}}(t)\boldsymbol{\mathcal{P}} & \boldsymbol{\mathcal{Q}}\boldsymbol{\mathcal{L}}(t)\boldsymbol{\mathcal{Q}}\end{bmatrix}\begin{bmatrix}\boldsymbol{p}(t)\\ \boldsymbol{\sigma}(t)\end{bmatrix}. \quad (28)$$

Similar to the procedure in Nakajima–Zwanzig equation,[38,56,57] we can obtain the equation of motion for $\boldsymbol{p}(t)$ as follows:

$$\dot{\boldsymbol{p}}(t) = \int_0^t d\tau\tilde{\boldsymbol{K}}(t-\tau;t)\boldsymbol{p}(\tau), \quad (29)$$

where the rate kernel $\tilde{\boldsymbol{K}}(t-\tau;t)$ can be expressed as:[38]

$$\tilde{\boldsymbol{K}}(t-\tau;t) = -\boldsymbol{\mathcal{P}}\boldsymbol{\mathcal{L}}(t)\boldsymbol{\mathcal{Q}}\boldsymbol{\mathcal{U}}(t,\tau)\boldsymbol{\mathcal{Q}}\boldsymbol{\mathcal{L}}(\tau)\boldsymbol{\mathcal{P}}. \quad (30)$$

In Eq. (31), we define the time-evolution operator $\boldsymbol{\mathcal{U}}(t,\tau)$ as:

$$\boldsymbol{\mathcal{U}}(t,\tau) \equiv \exp_+\left[-i\int_\tau^t d\tau'\boldsymbol{\mathcal{L}}(\tau')\right]. \quad (31)$$

It is worth noting that $-k(t-\tau;\ t)$ and $k'(t-\tau;\ t)$ in Eq. (25) correspond to the $|D\rangle\langle D| \to |D\rangle\langle D|$ and $|A\rangle\langle A| \to |D\rangle\langle D|$ components of $\tilde{\boldsymbol{K}}(t-\tau;t)$, respectively.

III. RESULTS AND DISCUSSIONS

A. Population rate without driving

If the system is time-independent, the forward and backward rate memory kernels, $k(t-\tau;\ t)$ and $k'(t-\tau;\ t)$, in Eq. (25) can

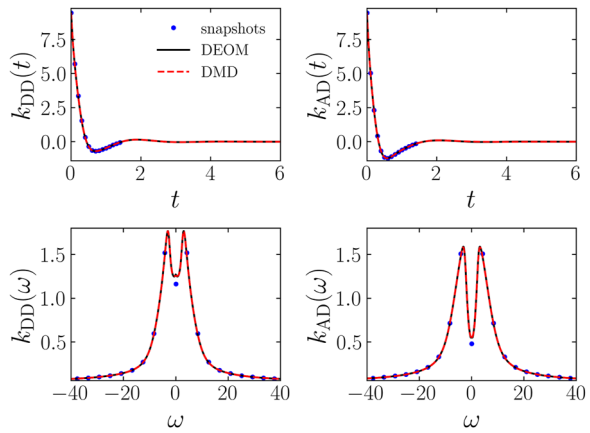

FIG. 1. The rate kernels $k_{DD/AD}(t)$ (upper panel) and their Fourier transformations $k_{DD/AD}(\omega)$ (lower panel), obtained through three methods: snapshots, DEOM, and DMD. $k_{DD}(t)$ and $k_{AD}(t)$ represent the rate kernels from the donor to the donor and the acceptor to the donor, respectively. Snapshots are obtained by sampling DEOM from $0 \le t \le 1.5$. This study utilizes a total of 150 snapshots. To ensure graph clarity, the snapshots are plotted every ten intervals. Based on the snapshots, DMD predicts kernels of the same length as DEOM. In reality, DMD has the capability to predict for any future time. However, for visualization purposes, the results are plotted only up to $t = 6$. The spectral density is represented by $J_D(\omega)$. H_S is defined as $\sigma_x + \sigma_z$, where σ refers to the Pauli matrices. The time step is $dt = 0.01$. Additionally, we have $\lambda = 1$, $\gamma = \omega_0 = \zeta = 1$ in our model. And we have kept $r = 8$ in the DMD calculations for both k_{DD} and k_{AD}.

be simplified as $k_{DD}(t-\tau)$ and $k_{AD}(t-\tau)$, respectively, due to the time–translation invariance. We first obtain a small number of snapshots of the rate kernels calculated by DEOM. Then the DMD is used to predict the remaining part based on these snapshots, as depicted in upper panel of Fig. 1.

Without an external field, we observe that both rate kernels $k_{DD}(t)$ and $k_{AD}(t)$ decrease to a value that slightly below zero, followed by an increase to a value slightly above zero, until ultimately approaching to zero. We see that DMD can accurately predict the rate kernels for short and long time, which agree with DEOM results completely. In lower panel of Fig. 1, we plot the Fourier transformation of the rate kernels. Notice that the spectral function of rate kernels predicted by the DMD is more accurate than that obtained directly from Fourier transform of the short time DEOM results, especially near $\omega = 0$. This is due to the fact that DMD provides accurate dynamics in longer time, which results in precise spectra near $\omega = 0$.

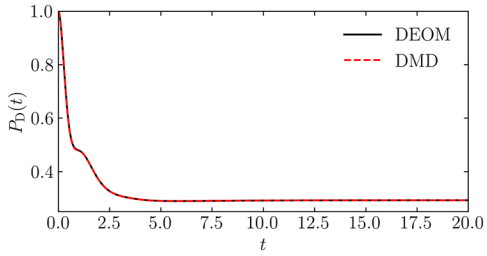

FIG. 2. The population of the donor, $P_D(t)$, is computed using the kernels depicted in Fig. 1 and Eq. (25). All the parameters used are identical to those in Fig. 1.

As a validation, we use the rate kernels namely $k_{DD}(t)$ and $k_{AD}(t)$ obtained through the DMD to calculate donor population $P_D(t)$ by Eq. (25). We also plot $P_D(t)$ obtained directly from DEOM calculation as a benchmark in Fig. 2. In the DMD calculation, we

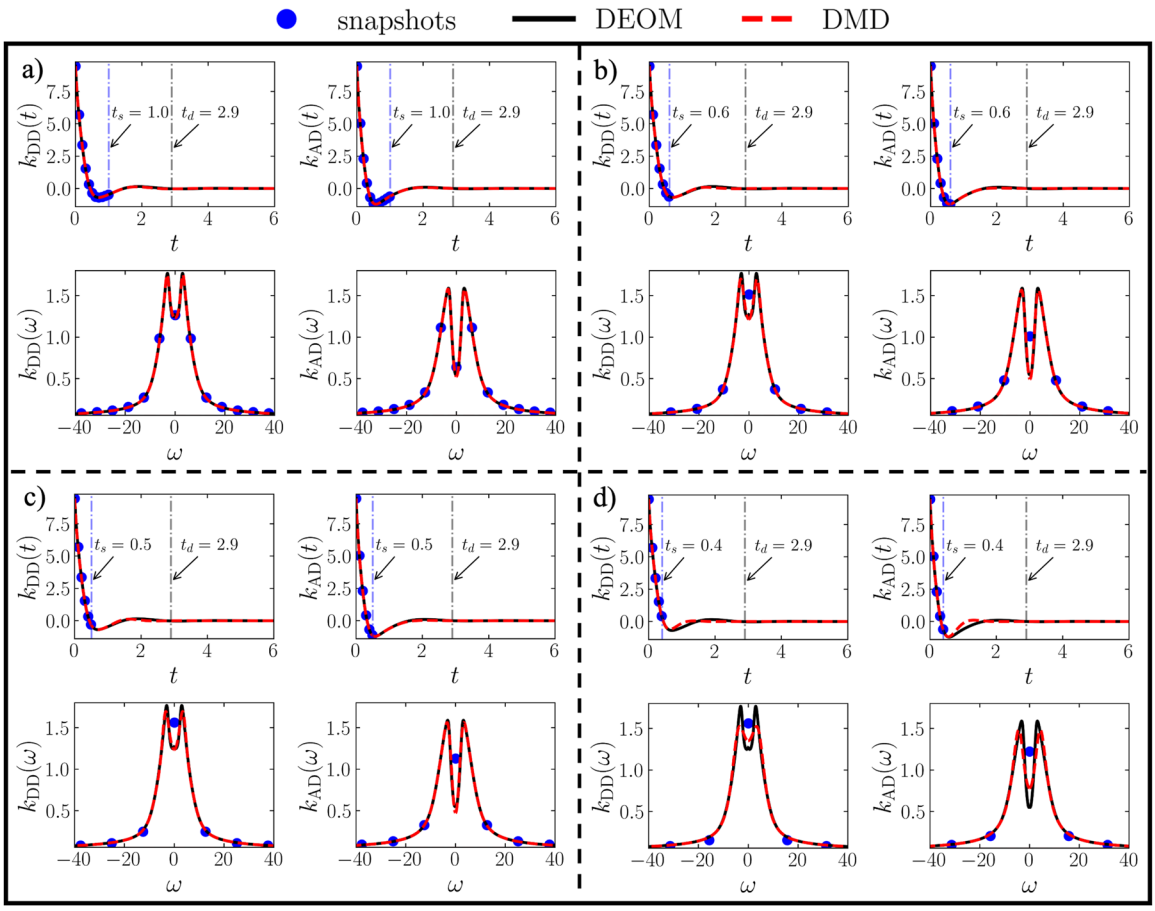

FIG. 3. The rate kernels $k_{DD/AD}(t)$ (upper panel) and their Fourier transformations $k_{DD/AD}(\omega)$ (lower panel), obtained through three methods: snapshots, DEOM, and DMD. t_d is the decay time of the kernels. t_s is the selected time of the snapshots, which is also the difference between subgraphs (a)–(d). $k_{DD}(t)$ and $k_{AD}(t)$ represent the rate kernels from the donor to the donor and the acceptor to the donor, respectively. Snapshots are obtained by sampling DEOM from $0 \le t \le t_s$ and the time step is $dt = 0.01$. To ensure graph clarity, the snapshots are plotted every ten intervals. The fewer snapshots used, the more inaccurate the DMD prediction results. When $t_s = 0.4$, DMD is significantly ineffective. The spectral density is represented by $J_D(\omega)$. H_S is defined as $\sigma_x + \sigma_z$, where σ refers to the Pauli matrices. Additionally, we have $\lambda = 1$, $\gamma = \omega_0 = \zeta = 1$ in our model. And we have $r = 8, 6, 6, 4$ in the DMD calculation for subgraphs (a)–(d) respectively.

have used 150 snapshots with $dt = 0.01$. We can see that DMD results agree with DEOM results perfectly. The DMD accuracy can be further enhanced if the number of snapshots are increased and the value of dt is decreased. Importantly, note that only a small number of snapshots for a short time of the rate kernels are required in DMD, such that DMD significantly reduces the overall computation cost.

In order to explore the efficiency limit of DMD, we selected different numbers of snapshots for the same calculations as Figs. 1 and 2. The results are shown in Figs. 3 and 4 with subgraphs (a)–(d) where t_d is the decay time of the kernels and t_s is the selected time of the snapshots. In Fig. 3, we can see that the fewer snapshots used, the more inaccurate the DMD prediction results. Especially, when $t_s = 0.4$, DMD is significantly ineffective. In Fig. 3, we can more clearly observe the deterioration process of DMD from the perspective of the population as the number of snapshots decreases. In some cases such as $t_s = 1.0$ or $t_s = 0.6$, DMD predicts longer-term evolution well when stable patterns exist. However, at $t_s = 0.4$, the DMD results fail completely, while at this moment, the kernel information covered by snapshots has lost crucial turning points. Now we can say that the number of snapshots cannot be continuously reduced, because to improve prediction accuracy, although snapshots need not extend to the scale of decay, they must encompass the essential information of the kernel. After all, DMD learns from data without a detailed model.

TABLE I. The efficiency of DMD compared to DEOM tested on one Mac M1 chip. The first column is the calculation time termination for kernels. The second column shows the proportion of improvement in computational efficiency by DMD compared to DEOM calculation and *speed up* = $(time_{\mathrm{DMD}}/time_{\mathrm{DEOM}}) * 100\%$. DMD calculation adopts $t_s = 0.6$. Considering fair comparison, $time_{\mathrm{DMD}}$ used here includes the time of the generation of snapshots.

t (a.u.)	Speed up (%)
1.50	32.1
2.90	46.3
20.0	70.5
100	78.7

To put a number on how efficient DMD calculations are, we calculate the proportion of improvement in computational efficiency by DMD compared to DEOM calculation tested on one Mac M1 chip as shown in Table I. For this example, DMD calculation adopts $t_s = 0.6$ and *speed up* = $(time_{\mathrm{DMD}}/time_{\mathrm{DEOM}}) * 100\%$. Considering fair comparison, $time_{\mathrm{DMD}}$ used here includes the time of the generation of snapshots. We can see that the longer the calculation time of the kernels, the greater the improvement in computational efficiency by DMD, from 32.1% saved when $t = 1.5$ to 78.7% saved when $t = 100$.

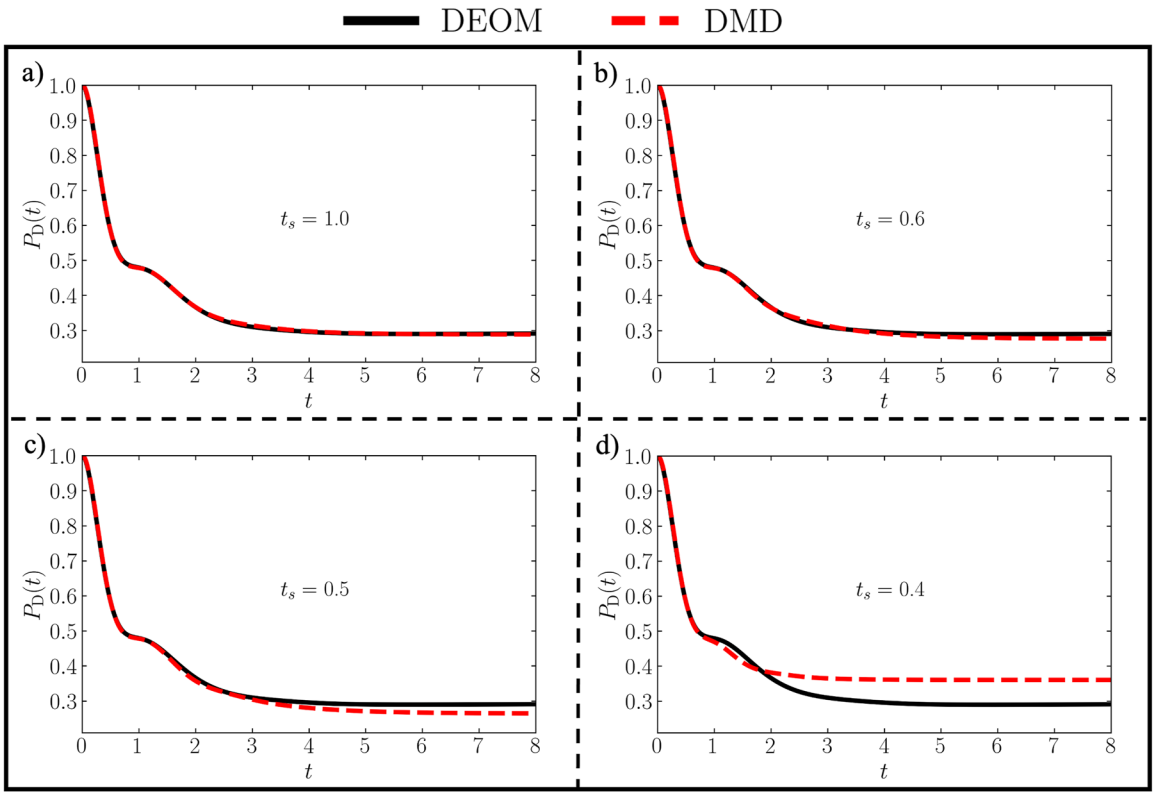

FIG. 4. The population of the donor, $P_{\mathrm{D}}(t)$, is computed using the kernels depicted in Fig. 3 and Eq. (25). All the parameters used are identical to those in Fig. 3. As the number of snapshots used decreases, the population of the donor obtained by DMD becomes increasingly inaccurate. When $t_s = 0.4$, the DMD results have become significantly invalid.

Additionally, DMD is capable of predicting observables for any future time. In other word, DMD doesn't require costly time-stepping computations, leading to higher efficiency.

B. Population rate with Floquet driving

If the system is Floquet-driven, the forward and backward rate memory kernels in Eq. (25) will satisfy

$$k(t-\tau;t+T_0)=k(t-\tau;t), \tag{32}$$

$$k'(t-\tau;t+T_0)=k'(t-\tau;t). \tag{33}$$

Here, $T_0=2\pi/\Omega$ is the period of the Floquet driving [cf. Eq. (20)]. We use k^{DD} and k^{AD} to denote the rate kernel from donor to donor k and acceptor to donor k', respectively. Obviously, $k^{\mathrm{DD}}(\tau;\ t)$ and $k^{\mathrm{AD}}(\tau;\ t)$ have two independent variables, τ and t. Due to the periodicity of the rate kernels, we perform a Fourier expansion on t,

$$k^{\mathrm{DD/AD}}(\tau;t)=\sum_{n=-\infty}^{\infty}k_n^{\mathrm{DD/AD}}(\tau)e^{in\Omega t}. \tag{34}$$

Here, the Fourier component $\{k_n^{\mathrm{DD/AD}}(\tau)\}$ is given by

$$k_n^{\mathrm{DD/AD}}(\tau)=\frac{1}{T_0}\int_0^{T_0}dtk^{\mathrm{DD/AD}}(\tau;t)e^{in\Omega t}. \tag{35}$$

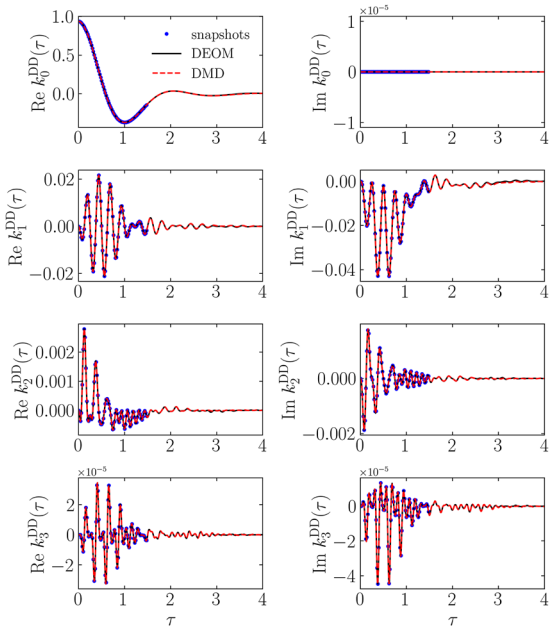

FIG. 5. The Fourier expansion terms of the kernel from donor to donor k_n^{DD} and $n=0,1,2,3$, obtained by three methods: snapshots, DEOM and DMD. Among them, snapshots are obtained by sampling of DEOM, and DMD predicts kernels of the same length as DEOM based on the snapshots. The spectral densities are $J_{\mathrm{D}}(\omega)$ and $J_{\mathrm{B}}(\omega)$, $dt=0.01$, and the number of snapshots is 150. Besides, $\varepsilon=2$, $\Omega=4, E^{\circ}=1.5, \lambda=\lambda'=0.2$ and $\gamma=\omega_0=\zeta=1$. We have $r=32,16,19,23$ in the DMD calculations for $n=0,1,2,3$ respectively.

Since the Fourier component approaches zero rapidly with increasing n, we only need to compute finite number of the Fourier components. Also, due to the symmetry $k_n^{\mathrm{DD/AD}}(\tau)=k_{-n}^{\mathrm{DD/AD}}(\tau)^*$, we only need to calculate Fourier components with $n\geq 0$.

We use $J_{\mathrm{D}}(\omega)$ in Eq. (23) and $J_{\mathrm{B}}(\omega)$ in Eq. (24) as spectral densities in the DEOM calculation and the initial state is on the donor. We utilize DMD to predict the Fourier components $k_n^{\mathrm{DD}}(\tau)$ and $k_n^{\mathrm{AD}}(\tau)$ based on the snapshots sampled from DEOM results as shown in Figs. 5 and 6, respectively. As we can see, unlike in the time-independent scenario, in the case where n is non-zero, the Fourier expansion terms of the rate kernels exhibit oscillation in both the real and imaginary parts. Furthermore, with increasing n, the magnitudes of the Fourier components decrease rapidly, ultimately converging to zero. Notice that even we do not sample $k_n(\tau)$ until convergence to zero, DMD can accurately predict long time behavior. This is due to the fact that the temporal frequencies and spatial modes can be extracted efficiently from the short time dynamics, such that DMD can predict future results with sufficiently small error. In our example, we have used only the snapshots within the range $0\leq t\leq 1.5$ with $dt=0.01$. Still, the predicted results obtained using DMD are nearly identical to those obtained using DEOM. This greatly reduces the overall amount of computation time.

To further verify our prediction, we substitute the values of $k_n^{\mathrm{DD/AD}}(\tau)$ obtained using DMD in Figs. 5 and 6 back into the rate

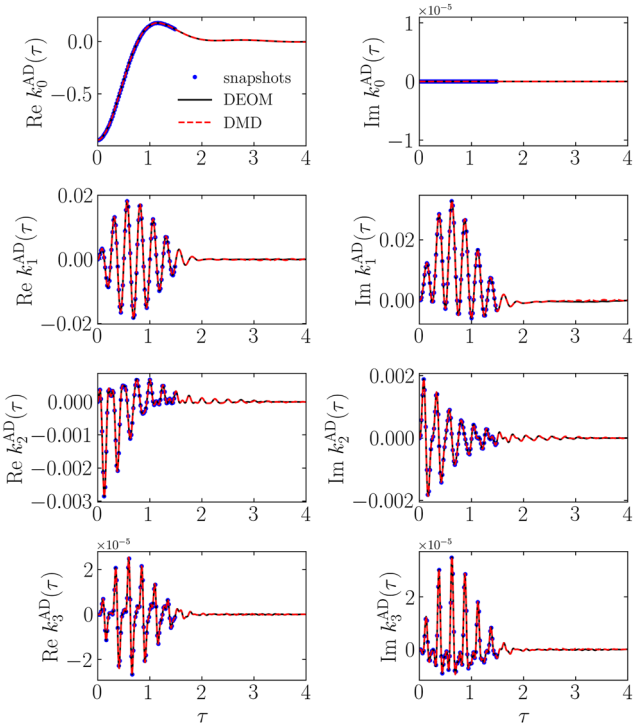

FIG. 6. The Fourier expansion terms of the kernel from acceptor to donor k_n^{AD} and $n=0,1,2,3$, obtained by three methods: snapshots, DEOM and DMD, with the same parameters used in Fig. 5. We have $r=30,22,19,24$ in the DMD calculations for $n=0,1,2,3$ respectively.

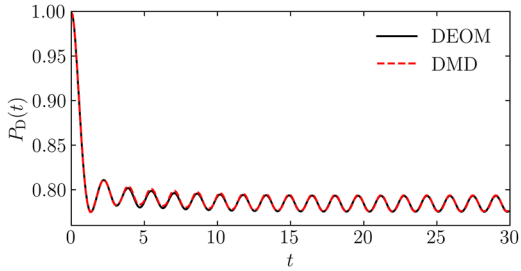

FIG. 7. The population of the donor $P_D(t)$ calculated using the kernels shown in Figs. 5 and 6 together with Eqs. (34) and (25). All the parameters are the same as those used in Fig. 5.

kernels [in Eq. (34)] and solve for donor population $P_D(t)$ [using Eq. (25)]. The results are illustrated in Fig. 7. Under the influence of Floquet driving, $P_D(t)$ reaches to a limit cycle instead of a steady state. The period of the limit cycle is equal to the period of the driving frequency. This proves that DMD can even predict long time behavior that is not a steady state. The accuracy of predicting the period of this oscillation mainly depends on the accuracy of DMD in predicting the imaginary part of $k_n^{DD/AD}(\tau)$, which jointly determines the range of ultimate convergence along with the real part of $k_n^{DD/AD}(\tau)$.

C. Density matrix evolution

In both Secs. III A and III B, we obtain $P_D(t)$ by integrating only the rate kennels. In this subsection, we utilize DMD to predict the complete kernel tensor $\mathcal{K}(t)$ and evolve the reduced density matrix $\rho(t)$ to obtain $P_D(t)$ and coherence evolution simultaneously. From Nakajima-Zwanzig formulation,[56,57] the equation of motion for the reduced density operator reads

$$\dot{\rho}(t) = -\mathrm{i}[H_S, \rho(t)] + \int_0^t d\tau \mathcal{K}(t-\tau)\rho(t), \tag{36}$$

where $\rho(t)$ is a 2-by-2 matrix that represents the reduced density operator for the donor and acceptor:

$$\rho(t) = \begin{bmatrix} \rho_{DD}(t) & \rho_{DA}(t) \\ \rho_{AD}(t) & \rho_{AA}(t) \end{bmatrix}, \tag{37}$$

and $\mathcal{K}(t)$ is the projected memory kernel.

Here, $\rho_{ij}(t)$ satisfies $\rho_{DD} + \rho_{AA} = 1$ and $\rho_{DA} = \rho_{AD}^*$. As a result, by denoting $K_{ij}[k,l] \equiv \langle\langle kl|\mathcal{K}|ij\rangle\rangle$, we have $K_{ij}[\mathrm{D,\ D}] = -K_{ij}[\mathrm{A,\ A}]$ and $K_{ij}[\mathrm{D,\ A}] = K_{ji}^*[\mathrm{A,\ D}]$. Therefore, we only need to calculate $K_{ij}[0,0] \equiv K_{ij}[\mathrm{D,\ D}]$ and $K_{ij}[0,1] \equiv K_{ij}[\mathrm{D,\ A}]$ in our simulations. We have used the Liouville-space projection operator approach in DEOM to calculate the memory kernels.[38]

As a example, we use the same time-independent system as in Sec. III A. We obtain 150 snapshots of the kernel tensors with $dt = 0.01$, calculated by DEOM using the spectral density $J_D(\omega)$ in Eq. (23) and the initial state is on the donor. We predict the

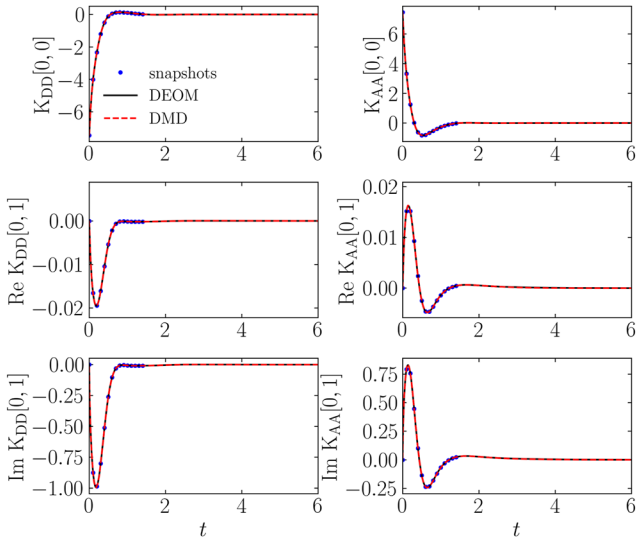

FIG. 8. The elements of kernel tensors for $K_{DD}[i,j]$ (left column) and $K_{AA}[i,j]$ (right column) obtained by three methods: snapshots, DEOM and DMD. $K_{DD/AA}[i,j]$ represents the i-th row and j-th column position of $K_{DD/AA}$ at every timestep. All the parameters in our model are the same as those used in Fig. 1. Additionally, in the DMD calculations, we have $r = 11$ for $K_{DD}[i,j]$ and $r = 15, 14, 10$ for $K_{AA}[0,0]$, Re $K_{AA}[0,1]$, and Im $K_{AA}[0,1]$.

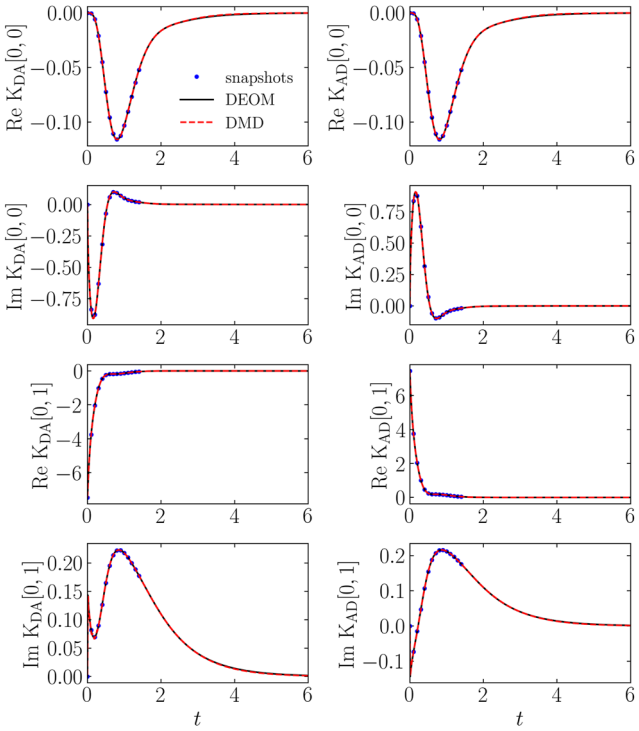

FIG. 9. The elements of kernel tensor for $K_{DA}[i,j]$ (left column) and $K_{AD}[i,j]$ (right column) obtained by three methods: snapshots, DEOM and DMD, with the same parameters in our model used in Fig. 1. Additionally, in the DMD calculations, we have $r = 7, 10, 22, 9$ for Re $K_{DA}[0,0]$, Im $K_{DA}[0,0]$, Re $K_{DA}[0,1]$, Im $K_{DA}[0,1]$ and $r = 7, 10, 20, 7$ for Re $K_{DA}[0,0]$, Im $K_{DA}[0,0]$, Re $K_{DA}[0,1]$, Im $K_{DA}[0,1]$, respectively.

kernels using DMD based on these snapshots as shown in Figs. 8 and 9. For all kernel tensors $K_{ij}[k,l](t)$, we see the DMD prediction agrees well with the DEOM calculation for both the real part and the imaginary part. We then assemble these kernel tensors into the generalized master Eq. (36) to calculate the time evolution of the density matrix. We plot the coherence $\rho_{\mathrm{DA}}(t)$ in Fig. 10 and the donor population $\rho_{\mathrm{DD}}(t)$ in Fig. 11. Note that the coherence is complex and DMD predicts both the real part and the imaginary part very well. In particular, the time-scale required for the imaginary part of the coherence approaching zero is the so-called decoherence time, which is captured well by DMD. Note that we have used the same parameters in Figs. 11 and 2, and the results are identical. Different from the generalized master equation, the rate kernels do not require the information of coherence. Nevertheless, the rate kernel methods give identical results as the generalized master equation.

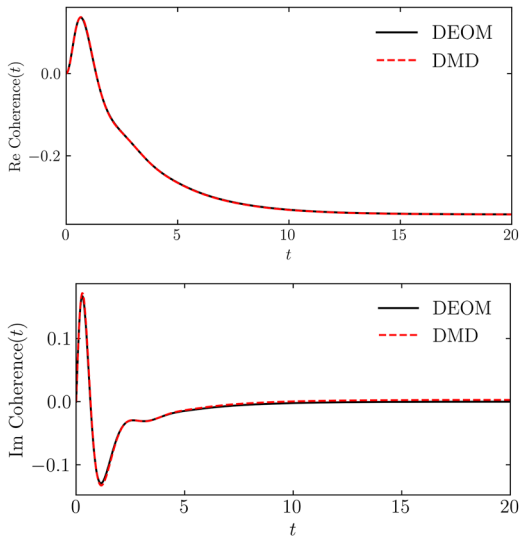

FIG. 10. The coherence between donor and acceptor obtained by DEOM and DMD using the kernel tensors in Figs. 8 and 9 together with Eq. (36), with the same parameters used in Fig. 1.

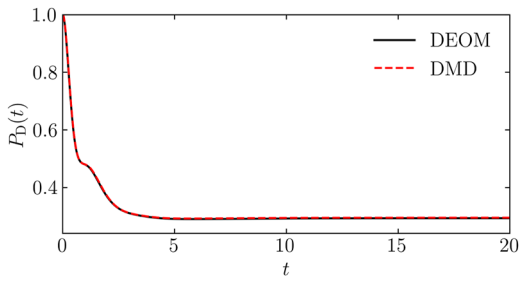

FIG. 11. The population of the donor $P_{\mathrm{D}}(t)$ obtained by DEOM and DMD, with the same parameters used in Fig. 1.

IV. CONCLUSIONS

To summarize, in this work, we exploit the DMD method to investigate the rate kernels in the simulation of open quantum systems. Traditional numerical methods to obtain the rate kernels involve solving coupled two-time nonlinear integral differential equations, which results in high memory requirement and large computational cost. In contrast, the data-driven DMD method only depends on a small sampled set of the numerical solutions, and can be easily applied through the truncated SVD decomposition. Our numerical results on the rate kernels of open quantum systems show that the DMD successfully captures the major dynamical modes and the frequencies of rate kernels, whether the external field is involved or not. Not limited to the specific forms of spectral density used in this article, DEOM can be used to describe arbitrary spectral density and anharmonic system potential as well. In addition, DEOM can be used to study Anderson model (one type of strong correlation model). DEOM can be very expensive to study the dynamics of Anderson model, especially in very low temperature, while DMD approach can be used to significantly reduce the computational cost in this case and this work is on-going. We anticipate that the DMD would become a useful tool for simulating dynamics of open quantum systems.

ACKNOWLEDGMENTS

We thank YiJing Yan for useful correspondence. W.D. acknowledges start-up funding from Westlake University.

AUTHOR DECLARATIONS

Conflict of Interest

The authors have no conflicts to disclose.

Author Contributions

Wei Liu: Investigation (equal); Writing – original draft (equal). **Zi-Hao Chen**: Software (equal). **Yu Su**: Software (equal). **Yao Wang**: Writing – review & editing (equal). **Wenjie Dou**: Writing – review & editing (equal).

DATA AVAILABILITY

The data that support the findings of this study are available from the corresponding author upon reasonable request.

REFERENCES

[1] P. J. Schmid, "Dynamic mode decomposition of numerical and experimental data," J. Fluid Mech. **656**, 5 (2010).
[2] C. W. Rowley, I. Mezić, S. Bagheri, P. Schlatter, and D. S. Henningson, "Spectral analysis of nonlinear flows," J. Fluid Mech. **641**, 115 (2009).
[3] J. H. Tu, "Dynamic mode decomposition: Theory and applications," Ph.D. thesis, Princeton University, 2013.
[4] J. N. Kutz, S. L. Brunton, B. W. Brunton, and J. L. Proctor, *Dynamic Mode Decomposition: Data-Driven Modeling of Complex Systems* (SIAM, 2016).

[5]K. K. Chen, J. H. Tu, and C. W. Rowley, "Variants of dynamic mode decomposition: Boundary condition, Koopman, and Fourier analyses," J. Nonlinear Sci. **22**, 887 (2012).
[6]L. Mejía, J. Yin, D. R. Reichman, R. Baer, C. Yang, and E. Rabani, "Stochastic real-time second-order Green's function theory for neutral excitations in molecules and nanostructures," arXiv:2303.06874 (2023).
[7]M. B. Plenio and P. L. Knight, "The quantum-jump approach to dissipative dynamics in quantum optics," Rev. Mod. Phys. **70**, 101 (1998).
[8]S. Jang, J. Cao, and R. J. Silbey, "Fourth-order quantum master equation and its Markovian bath limit," J. Chem. Phys. **116**, 2705 (2002).
[9]Q. Shi and E. Geva, "A new approach to calculating the memory kernel of the generalized quantum master equation for an arbitrary system–bath coupling," J. Chem. Phys. **119**, 12063 (2003).
[10]R.-X. Xu, P. Cui, X.-Q. Li, Y. Mo, and Y. Yan, "Exact quantum master equation via the calculus on path integrals," J. Chem. Phys. **122**, 041103 (2005).
[11]X.-Q. Li, J. Luo, Y.-G. Yang, P. Cui, and Y. Yan, "Quantum master-equation approach to quantum transport through mesoscopic systems," Phys. Rev. B **71**, 205304 (2005).
[12]L. Kidon, E. Y. Wilner, and E. Rabani, "Exact calculation of the time convolutionless master equation generator: Application to the nonequilibrium resonant level model," J. Chem. Phys. **143**, 234110 (2015).
[13]W. C. Pfalzgraff, A. Montoya-Castillo, A. Kelly, and T. E. Markland, "Efficient construction of generalized master equation memory kernels for multi-state systems from nonadiabatic quantum-classical dynamics," J. Chem. Phys. **150**, 244109 (2019).
[14]E. Mulvihill, A. Schubert, X. Sun, B. D. Dunietz, and E. Geva, "A modified approach for simulating electronically nonadiabatic dynamics via the generalized quantum master equation," J. Chem. Phys. **150**, 034101 (2019).
[15]G. Amati, M. A. Saller, A. Kelly, and J. O. Richardson, "Quasiclassical approaches to the generalized quantum master equation," J. Chem. Phys. **157**, 234103 (2022).
[16]J. B. Anderson, "Quantum chemistry by random walk: Higher accuracy," J. Chem. Phys. **73**, 3897 (1980).
[17]J. Kolorenč and L. Mitas, "Applications of quantum Monte Carlo methods in condensed systems," Rep. Prog. Phys. **74**, 026502 (2011).
[18]A. Lüchow, "Quantum Monte Carlo methods," WIREs Comput. Mol. Sci. **1**, 388 (2011).
[19]J. Carlson, S. Gandolfi, F. Pederiva, S. C. Pieper, R. Schiavilla, K. Schmidt, and R. B. Wiringa, "Quantum Monte Carlo methods for nuclear physics," Rev. Mod. Phys. **87**, 1067 (2015).
[20]P. P. Mazza, D. Zietlow, F. Carollo, S. Andergassen, G. Martius, and I. Lesanovsky, "Machine learning time-local generators of open quantum dynamics," Phys. Rev. Res. **3**, 023084 (2021).
[21]Y. Yan, "Theory of open quantum systems with bath of electrons and phonons and spins: Many-dissipaton density matrixes approach," J. Chem. Phys. **140**, 054105 (2014).
[22]H.-D. Zhang, R.-X. Xu, X. Zheng, and Y. Yan, "Nonperturbative spin–boson and spin–spin dynamics and nonlinear fano interferences: A unified dissipaton theory based study," J. Chem. Phys. **142**, 024112 (2015).
[23]H.-D. Zhang, R.-X. Xu, X. Zheng, and Y. Yan, "Statistical quasi-particle theory for open quantum systems," Mol. Phys. **116**, 780 (2018).
[24]Y. Wang, R.-X. Xu, and Y. Yan, "Entangled system-and-environment dynamics: Phase–space dissipaton theory," J. Chem. Phys. **152**, 041102 (2020).
[25]Y. Tanimura, "Nonperturbative expansion method for a quantum system coupled to a harmonic-oscillator bath," Phys. Rev. A **41**, 6676 (1990).
[26]Y. Tanimura, "Stochastic Liouville, Langevin, fokker–planck, and master equation approaches to quantum dissipative systems," J. Phys. Soc. Jpn. **75**, 082001 (2006).
[27]Y.-a. Yan, F. Yang, Y. Liu, and J. Shao, "Hierarchical approach based on stochastic decoupling to dissipative systems," Chem. Phys. Lett. **395**, 216 (2004).
[28]R.-X. Xu and Y. Yan, "Dynamics of quantum dissipation systems interacting with bosonic canonical bath: Hierarchical equations of motion approach," Phys. Rev. E **75**, 031107 (2007).
[29]J. Jin, X. Zheng, and Y. Yan, "Exact dynamics of dissipative electronic systems and quantum transport: Hierarchical equations of motion approach," J. Chem. Phys. **128**, 234703 (2008).
[30]H.-T. Chen and D. R. Reichman, "On the accuracy of surface hopping dynamics in condensed phase non-adiabatic problems," J. Chem. Phys. **144**, 094104 (2016).
[31]S. M. Blau, D. I. Bennett, C. Kreisbeck, G. D. Scholes, and A. Aspuru-Guzik, "Local protein solvation drives direct down-conversion in phycobiliprotein PC645 via incoherent vibronic transport," Proc. Natl. Acad. Sci. **115**, E3342 (2018).
[32]I. S. Dunn, R. Tempelaar, and D. R. Reichman, "Removing instabilities in the hierarchical equations of motion: Exact and approximate projection approaches," J. Chem. Phys. **150**, 184109 (2019).
[33]T. Ikeda and G. D. Scholes, "Generalization of the hierarchical equations of motion theory for efficient calculations with arbitrary correlation functions," J. Chem. Phys. **152**, 204101 (2020).
[34]L. P. Lindoy, A. Mandal, and D. R. Reichman, "Quantum dynamical effects of vibrational strong coupling in chemical reactivity," Nat. Commun. **14**, 2733 (2023).
[35]A. Ullah and P. O. Dral, "Speeding up quantum dissipative dynamics of open systems with kernel methods," New J. Phys. **23**, 113019 (2021).
[36]A. Ullah and P. O. Dral, "Predicting the future of excitation energy transfer in light-harvesting complex with artificial intelligence-based quantum dynamics," Nat. Commun. **13**, 1930 (2022).
[37]A. Kelly, A. Montoya-Castillo, L. Wang, and T. E. Markland, "Generalized quantum master equations in and out of equilibrium: When can one win?," J. Chem. Phys. **144**, 184105 (2016).
[38]H.-D. Zhang and Y. Yan, "Kinetic rate kernels via hierarchical Liouville–space projection operator approach," J. Phys. Chem. A **120**, 3241 (2016).
[39]A. Towne, O. T. Schmidt, and T. Colonius, "Spectral proper orthogonal decomposition and its relationship to dynamic mode decomposition and resolvent analysis," J. Fluid Mech. **847**, 821 (2018).
[40]N. Mohan, K. Soman, and S. Sachin Kumar, "A data-driven strategy for short-term electric load forecasting using dynamic mode decomposition model," Appl. Energy **232**, 229 (2018).
[41]B. O. Koopman, "Hamiltonian systems and transformation in Hilbert space," Proc. Natl. Acad. Sci. **17**, 315 (1931).
[42]B. O. Koopman and J. v. Neumann, "Dynamical systems of continuous spectra," Proc. Natl. Acad. Sci. **18**, 255 (1932).
[43]N. Takeishi, Y. Kawahara, and T. Yairi, "Learning Koopman invariant subspaces for dynamic mode decomposition," in *Advances in Neural Information Processing Systems* (NeurIPS, 2017), Vol. 30.
[44]S. Bagheri, "Computational hydrodynamic stability and flow control based on spectral analysis of linear operators," Arch. Comput. Methods Eng. **19**, 341 (2012).
[45]S. Bagheri, "Koopman-mode decomposition of the cylinder wake," J. Fluid Mech. **726**, 596 (2013).
[46]I. Mezić, "Analysis of fluid flows via spectral properties of the Koopman operator," Annu. Rev. Fluid Mech. **45**, 357 (2013).
[47]G. H. Golub and C. F. Van Loan, *Matrix Computations* (JHU press, 2013).
[48]Y. Su, Z.-H. Chen, H. Zhu, Y. Wang, L. Han, R.-X. Xu, and Y. Yan, "Electron transfer under the Floquet modulation in donor–bridge–acceptor systems," J. Phys. Chem. A **126**, 4554 (2022).
[49]U. Weiss, *Quantum Dissipative Systems* (World Scientific, 2012).
[50]H. Kleinert, *Path Integrals in Quantum Mechanics, Statistics, Polymer Physics, and Financial Markets* (World Scientific, 2009).
[51]Y. Yan and R. Xu, "Quantum mechanics of dissipative systems," Annu. Rev. Phys. Chem. **56**, 187 (2005).
[52]Z. Gong, Z. Tang, S. Mukamel, J. Cao, and J. Wu, "A continued fraction resummation form of bath relaxation effect in the spin-boson model," J. Chem. Phys. **142**, 084103 (2015).

[53]M. Xu, Y. Yan, Y. Liu, and Q. Shi, "Convergence of high order memory kernels in the Nakajima-Zwanzig generalized master equation and rate constants: Case study of the spin-boson model," J. Chem. Phys. **148**, 164101 (2018).
[54]Y. Yan, M. Xu, Y. Liu, and Q. Shi, "Theoretical study of charge carrier transport in organic molecular crystals using the Nakajima-Zwanzig-Mori generalized master equation," J. Chem. Phys. **150**, 234101 (2019).
[55]X. Dan, M. Xu, Y. Yan, and Q. Shi, "Generalized master equation for charge transport in a molecular junction: Exact memory kernels and their high order expansion," J. Chem. Phys. **156**, 134114 (2022).
[56]S. Nakajima, "On quantum theory of transport phenomena: Steady diffusion," Prog. Theor. Phys. **20**, 948 (1958).
[57]R. Zwanzig, "Ensemble method in the theory of irreversibility," J. Chem. Phys. **33**, 1338 (1960).